Check for updates

ADVANCED MATERIALS
www.advmat.de

Iridium-Based Selective Emitters for Thermophotovoltaic Applications

Gnanavel Vaidhyanathan Krishnamurthy, Manohar Chirumamilla,* Tobias Krekeler, Martin Ritter, Ragle Raudsepp, Mauricio Schieda, Thomas Klassen, Kjeld Pedersen, Alexander Yu. Petrov, Manfred Eich, and Michael Störmer*

The long-term operation of refractory-metal-based metamaterials is crucial for applications such as thermophotovoltaics. The metamaterials based on refractory metals like W, Mo, Ta, Nb, and Re fail primarily by oxidation. Here, the use of the noble metal Ir is proposed, which is stable to oxidation and has optical properties comparable to gold. The thermal endurance of Ir in a 3-layer-system, consisting of HfO_2/Ir/HfO_2, by performing annealing experiments up to 1240 °C in a pressure range from 2×10^{-6} mbar to 1 bar, is demonstrated. The Ir layer shows no oxidation in a vacuum and inert gas atmosphere. At temperatures above 1100 °C, the Ir layer starts to agglomerate due to the degradation of the confining HfO_2 layers. An in situ X-ray diffraction experimental comparison between 1D multilayered Ir/HfO_2 and W/HfO_2 selective emitters annealed at 1000 °C, 2×10^{-6} mbar, over 100 h, confirms oxidation stability of Ir while W multilayers gradually disappear. The results of this work show that W-based metamaterials are not long-term stable even at 1000 °C. However, the oxidation resistance of Ir can be leveraged for refractory plasmonic metamaterials, such as selective emitters in thermophotovoltaic systems with strong suppression of long wavelength radiation.

1. Introduction

Thermal stability of the emitter structures at high operating temperatures is essentially required to obtain high conversion efficiencies in thermophotovoltaic (TPV) energy-harvesting systems.[1–4] TPV is a direct method to convert thermal energy into electrical energy. In a TPV system, a thermal emitter is heated using a wide variety of sources. The heated emitter then emits electromagnetic energy in the form of thermal radiation, which will be converted into electricity using a photovoltaic, PV, cell.[5–7] The spectrally selective emitters[8–13] are tailored to emit radiation that matches the absorption spectrum of the PV cell used. According to Stefan–Boltzmann law, the power thermally radiated from a body is proportional to the T^4.[14,15] At the same time, due to the Wien displacement law, the spectral maximum of the body's thermal radiation is proportional to $1/T$, therefore, it shifts toward shorter wavelengths with increasing temperature. Hence, elevating the emitter temperature significantly boosts the radiative power and conversion efficiency if used in conjunction with matched wide-bandgap PV cells noted for their large open-circuit voltage, such as InGaAsSb, GaSb, Ge, InGaAs, etc.[5,14]

Alternative to selective emitters, a broadband reflector can be integrated under the PV cell to send unabsorbed long wavelength radiation back to the emitter. Currently, the state-of-the-art TPV system efficiency of 41% is demonstrated with a broadband thermal emitter at 2400 °C, paired with a transparent two-junction PV cell and a reflective Au mirror positioned behind the PV cell.[16] However, maintaining such elevated temperatures in an operating system for a long-time is a challenge. Reduction of the temperature to

G. Vaidhyanathan Krishnamurthy, R. Raudsepp, M. Schieda, A. Y. Petrov, M. Eich, M. Störmer
Institute of Photoelectrochemistry
Helmholtz-Zentrum Hereon
Max-Planck-Strasse 1, 21502 Geesthacht, Germany
E-mail: gnanavel.vaidhyanathan@hereon.de

M. Chirumamilla, A. Y. Petrov, M. Eich
Institute of Optical and Electronic Materials
Hamburg University of Technology
Eissendorfer Strasse 38, 21073 Hamburg, Germany
E-mail: mch@mp.aau.dk

M. Chirumamilla, K. Pedersen
Department of Materials and Production
Aalborg University
Skjernvej 4A, 9220 Aalborg Øst, Denmark

T. Krekeler, M. Ritter
Electron Microscopy Unit
Hamburg University of Technology
Eissendorfer Strasse 42, 21073 Hamburg, Germany

T. Klassen
Institute of Hydrogen Technology
Helmholtz-Zentrum Hereon
Max-Planck-Strasse 1, 21502 Geesthacht, Germany

The ORCID identification number(s) for the author(s) of this article can be found under https://doi.org/10.1002/adma.202305922

© 2023 The Authors. Advanced Materials published by Wiley-VCH GmbH. This is an open access article under the terms of the Creative Commons Attribution License, which permits use, distribution and reproduction in any medium, provided the original work is properly cited.

DOI: 10.1002/adma.202305922

1000–1300 °C leads to a drop of the efficiency below 30%.[7,17–20] In this case, even a typical reflector loss of 5% becomes problematic as the blackbody spectrum has most of its power in the long wavelength range. Thus using a reflector and PV cell with selective emitters can further enhance the TPV system efficiency and additionally reduce the thermal load on the PV cell.

In the quest for alternatives to selective emitters based on refractory metals, all-dielectric filters are proposed.[21–24] Recently, McSherry et al.,[21] highlighted the usage of an epitaxial heterostructure made of perovskite $BaZr_{0.5}Hf_{0.5}O_3$ and rocksalt MgO as a filter for low-energy photons, proving the thermal stability at high working temperatures of 1100 °C in an air atmosphere. But to achieve broadband suppression of long wavelength radiation, thick multilayers approaching 100 µm thickness would be required, which are technically challenging. In contrast, metal-based layered metamaterials have sub-micrometer thicknesses.[25–27]

Several previous researchers have reviewed the fundamental principles and results in thermophotovoltaics, extending to the present day.[4,13,28–32] In TPV, spectrally selective emitters consisting of photonic crystals, gratings, and multilayered metamaterials made of alternating metal and dielectric layers are employed to restrain low-energy out-of-band photons.[4,12,13,25,28,29,32–41] To date, a 1D metamaterial emitter exhibits the highest thermal stability at 1400 °C for 6 h.[38] Yet, the enduring thermal resilience of the emitters operating at 1400 °C remains uncertain. Nonetheless, most of the state-of-the-art TPV emitters are designed to function in the range of 1000 °C and higher. These emitters are paired with PV cells that possess a bandgap of 0.5–0.75 eV.[7,13,18,19,30,37,42,43] PV cells with bandgaps of 0.35 to <0.5 eV tend to suffer from recombination losses, adversely affecting their efficiency.[8,23,32,44] It is not viable to use far-field TPV systems based on selective emitters operating below 1000 °C as there is a significant reduction of emitted power and efficiency.[17,19,30,45,46] The efficiency drops drastically due to a large amount of long wavelength radiation, the underperformance of required low-bandgap PV cells, and limitations due to Carnot efficiency. Moreover, to ensure optimal performance from a PV cell, maintaining its low temperature is paramount. Techniques like circulating cold water or using passive cooling can be effectively employed.[47]

The potential heat sources for TPV include solar radiation, chemical and nuclear[48] processes, industrial waste heat,[31,49,50] remote power generation,[51,52] and combustion of hydrocarbon fuels.[53–55] Additionally, chip-scale TPV is on the rise with the progress in micro-scale heat sources.[56–58] With the present state-of-the-art TPV efficiency exceeding 30%, TPVs present significant advantages over thermoelectric generators, with efficiencies <6%, in, for example, remote power generation applications like deep-space and deep-sea explorations.[59–61] In recent developments, there has also been a surge in TPV-based thermal batteries. In these systems, heat energy stored at a grid scale, derived from renewable electricity, is converted by TPV back into electricity to meet demands during peak times.[62–65]

Selecting the suitable material to operate at such high working temperatures is crucial as thermally activated processes like grain growth, grain boundary migration, diffusion of defects, oxidation, and high-temperature corrosion come into play.[66–68] Refractory metals with high melting points like W, Mo, Ta, Nb, and TiN are often the first choice of materials to sustain high operating temperatures.[69–77] Despite their high melting point, at a medium vacuum pressure of 10^{-2} mbar, they are prone to rapid oxidation at high temperatures above 1000 °C,[25,38,78] resulting in the formation of volatile oxides that sublimate spontaneously, failing to meet long-term durability requirements. Therefore, most metals require demanding vacuum pressure conditions: that is, a low pressure, $<10^{-5}$ mbar, to reduce the O_2 partial pressure.[13,38] The alternate choice of materials to overcome oxidation at medium vacuum pressure are noble metals like Pt, Rh, Pd, Au, and Ir because of their better resistance to oxidation than non-noble metals. Nonetheless, Pt and Au are limited in application because of their relatively low melting points. The ideal choice among the noble metals is Ir, due to its high melting point of 2443 °C and its low vapor pressure of 1×10^{-8} mbar at 1763 °C.[79,80] The electronic configuration of Ir is (Xe) $4f^{14}$ $5d^7$ $6s^2$. Due to the poor shielding offered by the d-orbitals, the valence electrons of Ir are relatively close to the nucleus, causing them to be tightly bound and not readily available for any reactions.[81]

The superiority of Ir over other refractory metals with a very high melting point like W in the temperature range above 1000 °C is based on the following thermodynamic consideration. The Gibbs energy of formation ΔG_f, for IrO_2 is $\Delta G_f = -18.8$ kJ mol^{-1},[82] very low in comparison to other refractory metals, for example, W, where the formation of $WO_{2.7}$ is $\Delta G_f = -477.9$ kJ mol^{-1} at 1000 °C and 1 bar pressure. And it becomes positive shortly above 1000 °C, making an oxide formation thermodynamically unfavorable.[82] Therefore, in contrast to other refractory metals, the oxidation of Ir will be slow at low temperatures or could even be inhibited at high temperatures. High-temperature experiments on bulk Ir at different pressures and temperature ranges between 600–2000 °C, reveal different oxidation processes of Ir.[83–89] It was reported that at 1 bar pressure and above 600 °C, the solid oxide IrO_2 is formed and it is stable up to 1100 °C.[88] On increasing the temperature further, IrO_2 transforms into IrO_3, which exists only in a gaseous state, therefore it sublimates rapidly, leaving behind a fresh metal surface. Since oxidation of Ir still would consume metal at temperatures below 1000 °C, it is crucial to inhibit the formation of IrO_2 in the first place. This is achieved in our experiments by working in a vacuum pressure equal or below 2×10^{-2} mbar or in an inert gas atmosphere. Ir exhibits a negative real part of the complex dielectric permittivity in the visible and infrared (IR) range,[33,90–92] which is comparable to Au and Ag. In the mid-IR range, the reflectivity of Ir is approaching that of Au and Ag.[91]

In this work, we demonstrate the oxidation-resistant nature of Ir through high-temperature in situ and ex situ annealing experiments. In situ, annealing experiments are conducted at a vacuum pressure of 2×10^{-6} mbar and in the temperature range between 900–1240 °C on two structures: 1) a 3-layer system, consisting of HfO_2: 100 nm/Ir: 30 nm/HfO_2: 100 nm/substrate); 2) a bilayer system, consisting of Ir:30 nm/HfO_2:100 nm/substrate. Various investigations are performed to trace polymorphic phase transformation, solid-state reactions, and reaction kinetics as a function of time. Ex situ annealing experiments are done on a 3-layer system at three different pressures 1 bar, 2×10^{-2} mbar (technical vacuum condition), and 2×10^{-5} mbar, between 1000–1400 °C to validate structure and microstructure of Ir after different

© 2023 The Authors. Advanced Materials published by Wiley-VCH GmbH

15214095, 2023, 41, Downloaded from https://onlinelibrary.wiley.com/doi/10.1002/adma.202305922 by Technische Universität Hamburg Bibliothek - Elektronische Medien, Wiley Online Library on [23/11/2023]. See the Terms and Conditions (https://onlinelibrary.wiley.com/terms-and-conditions) on Wiley Online Library for rules of use; OA articles are governed by the applicable Creative Commons License

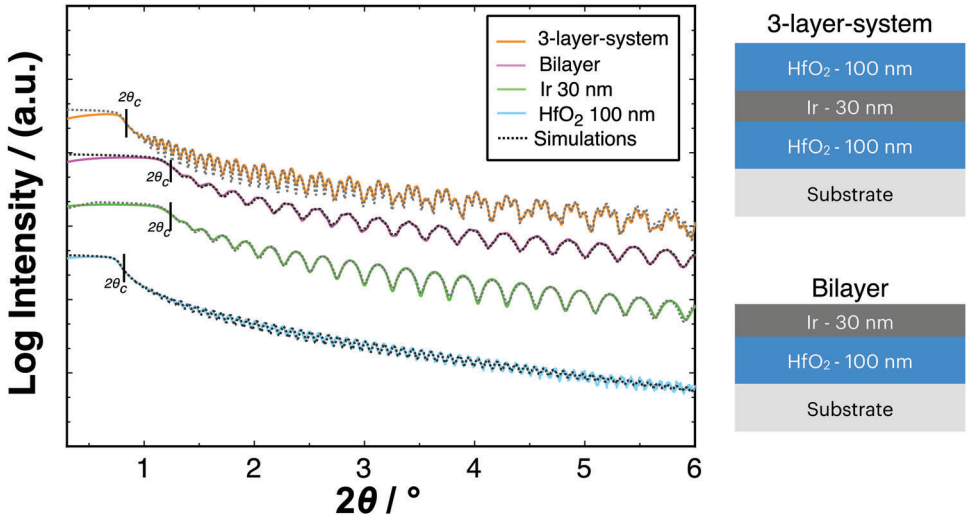

Figure 1. Measured and simulated XRR as a function of the scattering angle 2θ of as-prepared single 100 nm-thick HfO_2 layer, single 30 nm-thick Ir layer, bilayer (30 nm Ir/100 nm HfO_2), a 3-layer system (100 nm HfO_2/30 nm Ir/100 nm HfO_2) and each combination is simulated. On the right to the scans, schematics of the bilayer and 3-layer systems are shown.

annealing durations up to 100 h. These experimental results present new insight into the thermal endurance of Ir selective emitters under a practical working environment for TPV applications.

2. Results and Discussion

The schematics in **Figure 1** present a 3-layer (i.e., 100 nm HfO_2/30 nm Ir/100 nm HfO_2), and a bilayer (i.e., 30 nm Ir/100 nm HfO_2) systems. Magnetron sputtering[93,94] is a suitable method for depositing thin films of high melting point materials like Ir and HfO_2, and the technique is scalable and can be transferred from lab environments to industrial applications. Salient properties of the deposited layers like layer thickness, roughness, and density are determined using X-ray reflectivity (XRR). In Figure 1, four typical XRR scans using Cu $K_{\alpha 1}$-radiation with a wavelength of $\lambda = 0.15406$ nm and at scattering angles of 2θ from 0° up to 6° are shown for a 3-layer system, a bilayer system, and for two single layers of metallic Ir and dielectric HfO_2. First so-called Kiessig fringes are clearly visible in these scans,[95,96] which are a measure of the layer thickness. A 100 nm-thick HfO_2 layer causes short-period oscillations, while a 30 nm-thin Ir layer exhibits long-period oscillations. Furthermore, the decay of the logarithmic specular X-ray intensity is mainly determined by the roughness of the layers, which is in the sub-nanometer range for all layers. The critical angle θ_c for total external reflection of X-rays is directly related to the layer density,[97] therefore the θ_c of Ir is higher than the one from HfO_2 due to higher density. Simulated data generated by a genetic algorithm[98] for analysis of the measured XRR scans after using LEPTOS (Bruker AXS) software are listed in **Table 1**. At smaller angles of incidence, X-ray reflectometry is a powerful surface-sensitive analytical technique, but at higher angles and deeper penetration, X-ray diffraction (XRD) provides further thin-film properties such as structure, interplanar spacing, phase formation and transformation, and microstructure, which are essential for materials science of thin films.

In high-temperature materials research, in situ X-ray diffraction serves as an appropriate characterization technique by recording sequential diffraction patterns under controlled heating rates and at distinct vacuum pressures as a function of time and temperature, which helps us to investigate the thermal and temporal modification in the samples. A waterfall plot of a 3-layer system during the ramp and isothermal stages of the annealing experiment under a vacuum pressure of 2×10^{-6} mbar is shown in **Figure 2**. The diffractograms in blue represent the temperature ramp from room temperature until 1000 °C. No dominant peaks are visible from the HfO_2 layer measured at room temperature (first blue scan). A quantitative analysis using Bruker EVA software, which works on the principle of integral index method and utilizes X-ray diffraction data to determine the degree of crystallinity,[99,100] reveals that 90% of the HfO_2 layer is amorphous and 10% is monoclinic (Figure S1, Supporting Information). The prominent (111) peak at 40.3° belongs to the FCC phase of Ir. A longer offset coupled θ–2θ scan exhibits the higher-order peak (222) at 80.0° (not shown here). On further ramping up the temperature, HfO_2 undergoes a polymorphic phase transformation.[94] The amorphous phase initially transforms at 200 °C to a metastable tetragonal phase with a (101) reflection at 30.3°. Above 800 °C, the tetragonal phase transforms into the thermodynamically stable monoclinic phase with some new X-ray peaks, which are indexed by (−111) and (111). Compared to HfO_2, no phase transition is visible in the Ir layer. The peak at

Table 1. Simulated thickness, roughness, and densities of a single layer Ir and HfO_2 after analysis of the measured XRR scans. The experimental error of thickness determination is ±0.5 nm.

Layer	Thickness [nm]	Roughness [nm]	Density [g cm^{-3}]
Ir	30.4	0.25	22.3
HfO_2	100.1	0.27	9.4

© 2023 The Authors. Advanced Materials published by Wiley-VCH GmbH

15214095, 2023, 41, Downloaded from https://onlinelibrary.wiley.com/doi/10.1002/adma.202305922 by Technische Universität Hamburg Bibliothek - Elektronische Medien, Wiley Online Library on [23/11/2023]. See the Terms and Conditions (https://onlinelibrary.wiley.com/terms-and-conditions) on Wiley Online Library for rules of use; OA articles are governed by the applicable Creative Commons License

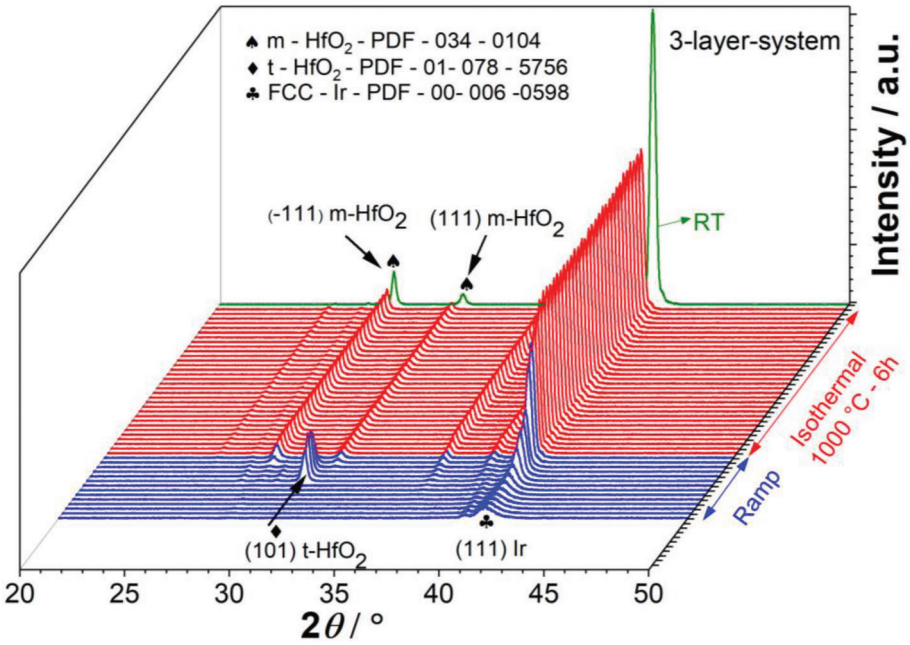

Figure 2. In situ XRD diffractograms of a 3-layer system from room temperature up to 1000 °C represented in blue. Diffractograms in red represent isothermal annealing at 1000 °C for 6 h at 2×10^{-6} mbar. The last scan in green is measured at room temperature at the end of the annealing experiment.

36.6° is due to Cu-K_β radiation from the (111) Ir peak. Clearly, there is a gradual increase in the intensity of the (111) peak during the temperature ramp that is accompanied by an initial decrease of the interplanar spacing d_{111} due to the relaxation process. Later a shift occurs to higher values due to thermal expansion (Figure S2, Supporting Information).

The diffractograms in red (3-layer system) represent the isothermal part of the annealing experiment at 1000 °C for 6 h. The first observation reveals no change in the peak intensity of HfO_2 compared to the last scan of the annealing ramp, which confirms the good condition of this refractory thin-film material, whereas the intensity of (111) FCC Ir peak in the 3-layer system continues to grow for a few minutes and then stabilizes at a constant level, as indicated by a turquoise arrow for the rest of the annealing period. No new peaks emerge in the isothermal annealing, confirming neither oxidation of the Ir layer, nor any possible reactions between Ir and HfO_2, and the absence of any chemical reaction between the bottom HfO_2 layer and the sapphire substrate. It is also worthwhile to compare the peak integral of (111) FCC Ir for room temperature diffraction patterns taken before and after annealing the 3-layer system. The area under the broad peak before annealing is small, as a result of a small grain size of ≈12 nm, and large defect concentration due to magnetron sputtering, whereas after annealing, the area under (111) FCC Ir peak is raised and the grain size increases to 30 nm due to grain coarsening and reduction of defects in the layer. The last scan in the waterfall plot highlighted in green is recorded after cooling the sample back to room temperature. The difference in intensity between the final room temperature and isothermal annealing scans is due to temperature-diffusive scattering (Figure S3, Supporting Information).

The evolution of the grain size of the annealed 3-layer system as a function of time and temperature is shown in **Figure 3**A,B. The grain size in the out-of-plane direction in the 30 nm-thick Ir layer is calculated better using the Scherrer formula,[101]

$$t = \frac{K\lambda}{B\cos\theta_B} \quad (1)$$

where t is the grain size, K is a dimensionless shape factor ($K = 0.89$ based on Gaussian line profiles and small cubic crystals of uniform size[101]), λ is the wavelength of X-rays (for Cu_α radiation: $\lambda = 0.15046$ nm), B is the full width at half maximum of the peak in radians, θ_B is the glancing angle in radians, which is half of the Bragg angle. The grain size of Ir in the as-prepared 3-layer system is ≈12 nm indicating it is nanocrystalline.[102–105] Above 250 °C, the grain size approaches a value of ≈30 nm and remains constant throughout the whole annealing ramp for all applied annealing temperatures up to 1240 °C (Figure 3A). The further increase of the diffraction peak intensity for temperatures above 250 °C as observed in Figure 2, can be attributed to the lateral grain growth induced by thermally activated mobility of the atoms and defects (such as twins and stacking faults). Nevertheless, the growth of the grains does not generate interface roughness between the Ir and HfO_2 layers. In the isothermal part of the annealing, also distinct changes in out-of-plane grain growth at different temperatures become apparent. The grain size of Ir saturates first at the original layer thickness of 30 nm for the 3-layer system during isothermal annealing up to 1000 °C for 6 h. This experimental result serves as a basis for the later described comparison between Ir and W-based multilayered metamaterial at 1000 °C. However, further grain growth is observed in the 3-layer system annealed at 1100 and 1240 °C, reaching values close to 50 nm linearly after 6 h of isothermal annealing (Figure 3B), which is significantly higher than the original layer thickness of 30 nm.

© 2023 The Authors. Advanced Materials published by Wiley-VCH GmbH

15214095, 2023, 41, Downloaded from https://onlinelibrary.wiley.com/doi/10.1002/adma.202305922 by Technische Universität Hamburg Bibliothek - Elektronische Medien, Wiley Online Library on [23/11/2023]. See the Terms and Conditions (https://onlinelibrary.wiley.com/terms-and-conditions) on Wiley Online Library for rules of use; OA articles are governed by the applicable Creative Commons License

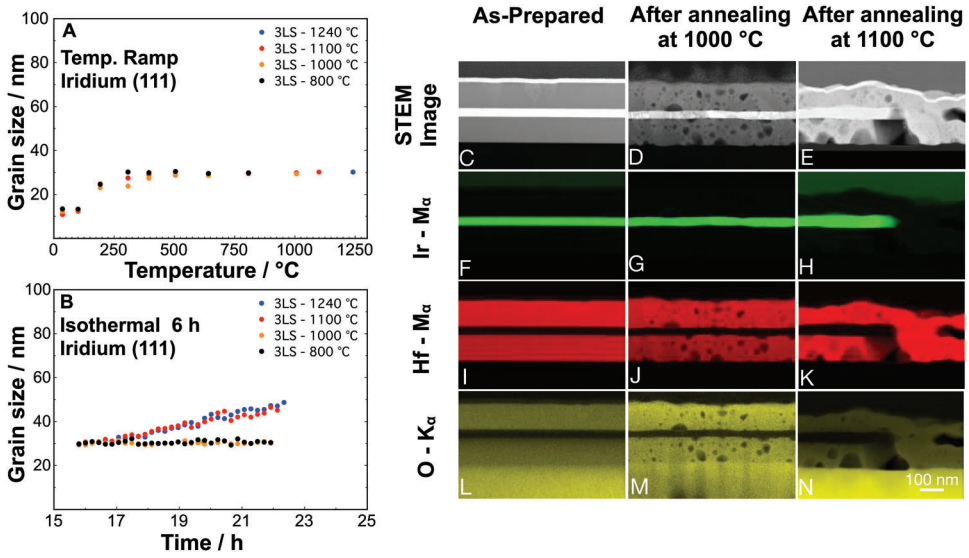

Figure 3. A,B) Measured out-of-plane grain size of FCC Ir as a function of temperature during the annealing ramp (A) and as a function of time during isothermal annealing (B) in the 3-layer system; calculated from the FWHM of the (111) peak of the FCC Ir phase. C–E) Cross-sectional STEM-HAADF images of the 3-layer system for as-prepared, annealed at 1000 and 1100 °C for 6 h at 2×10^{-6} mbar. F–N) The corresponding EDS mappings for Ir-M_α, Hf-M_α, O-K_α. All the images have the same scale as indicated in (N).

In order to interpret the increased grain growth of Ir in the 3-layer system at higher annealing temperatures, STEM-EDS characterization on the as-prepared and annealed samples, at 1000 and 1100 °C, was performed. A Cross-sectional STEM high-angle annular dark-field (STEM-HAADF), image, and the elemental mapping, Figure 3C,F,I,L, of the as-prepared sample show a 3-layer system with a smooth interface between Ir and HfO_2. The top layer is coated with a layer of Au in order to circumvent the effect of charging. After annealing at 1000 °C for 6 h, no noticeable change in the Ir layer is observed except grain growth-induced structural changes, but some voids and larger grains are seen in the HfO_2 layer. As seen in Figure 3D,J,M, the interface between Ir and HfO_2 layers appears to be unaltered. After annealing at 1100 °C for 6 h, drastic changes in the film morphology occur, Figure 3E. The Ir layer is not continuous anymore, and it is interrupted by the HfO_2 layer, a change in thickness of the Ir layer is also visible. The Ir layer is thicker than before on the left side of Figure 3H, while on the other side, the Ir has vanished. The EDS mapping of Ir shows a strong signal from Ir-M_α, and no presence of oxidation, where the metallic layer is visible. Likewise, the HfO_2 layer contains only signals from Hf-M_α and O-K_α, which confirms no sign of interdiffusion between the Ir and HfO_2.

To investigate the influence of the top HfO_2 layer in relation to the thermal stability of the 3-layer system, agglomeration, and grain size evolution of bilayers, that is, without the HfO_2 layer on the top, were observed after annealing by conductive atomic force microscopy (c-AFM). **Figure 4**A shows the top morphology of the as-prepared bilayer system with a roughness in the sub-nanometer range as determined before by XRR. The green line is the scan line of the height profile before annealing, shown in Figure 4D. The morphology of the annealed bilayer at 1000 °C, Figure 4B, shows no more a continuous Ir layer, instead, it is now an agglomeration of Ir into net-like structures on the former fully covered HfO_2 layers. The height profile along the pink line shown in Figure 4D exhibits two plate-like islands with widths of 300–900 nm. The surface roughness on top of the Ir islands is low, whereas between the islands the surface roughness of HfO_2 is ≈15–20 nm. The step height of the Ir islands is in the range of 60–100 nm, which is in good agreement with the calculated out-of-plane grain size from the measured XRD patterns. Figure 4C shows the current measurements over the net-like structures from the same surface area. The morphology is modified such that the metallic or conductive and the dielectric or insulating regions are exposed.

The loss of cohesion of the uppermost layer of the bilayer is due to the agglomeration of Ir, which starts from 900 °C, Figure S4 (Supporting Information). Here, the driving force for agglomeration[106] is to minimize the total energy of the free surfaces of Ir and the Ir–HfO_2 interface. In general, thin metal films deposited on an oxide surface are metastable and reduce interface area by forming islands by surface diffusion. Surface diffusion becomes significant at $\approx 0.5 T_m$, called the Tammann temperature[107] indicating the onset of the diffusive motion of the outermost atoms of a metallic region. Due to thermal treatment, the agglomeration proceeds by void formation as shown in Figure S5 (Supporting Information). The formed voids then grow to form dewetted regions that coalesce, resulting in dewetting of the entire film, Figure S6 (Supporting Information). Nevertheless, in the 3-layer system, the top HfO_2 layer stabilizes the structure. The additional Ir–HfO_2 interface prevents the agglomeration in the Ir layer up to 1000 °C, which demonstrates that Ir–HfO_2 is a competitive system for TPV metamaterials.

In the next part, the 3-layer system was ex situ annealed to verify the impact of O_2 partial pressure on the oxidation of Ir. **Figure 5**A shows diffractograms of a 3-layer system measured at room temperature after annealing at 1000 °C for 6 h under 1 bar (in air), 2×10^{-2} mbar, and 2×10^{-5} mbar vacuum pressures. The prominent peaks are (−111), (111), (211), (220), and (−122) from

© 2023 The Authors. Advanced Materials published by Wiley-VCH GmbH

15214095, 2023, 41, Downloaded from https://onlinelibrary.wiley.com/doi/10.1002/adma.202305922 by Technische Universität Hamburg Bibliothek - Elektronische Medien, Wiley Online Library on [23/11/2023]. See the Terms and Conditions (https://onlinelibrary.wiley.com/terms-and-conditions) on Wiley Online Library for rules of use; OA articles are governed by the applicable Creative Commons License

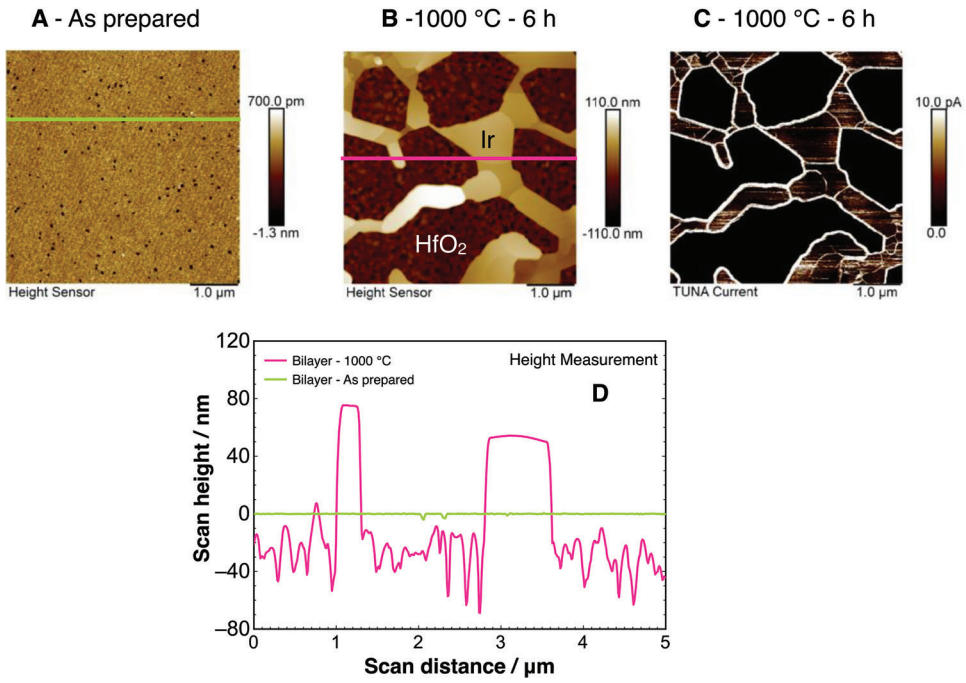

Figure 4. A,B) AFM images of as-prepared surface morphology of the Ir top layer of bilayer Ir/HfO_2 (A) and the surface of the same sample after annealing at 1000 °C for 6 h at 2×10^{-6} mbar showing agglomeration of Ir into net-like structures (B), and C) conductive AFM-image of the same sample after annealing, showing the flow of current from the net like structures of Ir, while the bottom HfO_2 layer is non-conducting. D) Height profile of the bilayer before and after annealing (green and pink lines in A and B, respectively).

monoclinic HfO_2, and the (111) FCC peak from Ir. In Figure S7 (Supporting Information), a thermodynamic analysis of the oxidation of Ir is conducted to map out the influence on the basis of minimization of the Gibbs free energy at different temperatures and vacuum pressures (known as an Ellingham diagram[108]). These considerations under thermodynamic equilibrium explain our experimental results consistently, because the conditions for oxidation of Ir are not reached here. Thus, there is no hint of IrO_2 peaks in the diffractograms after annealing at 2×10^{-2} mbar, and 2×10^{-5} mbar vacuum pressures. But, at 1 bar after 6 h, a clear drop of Ir peak is observed, which is attributed to the loss of Ir by sublimation of volatile oxides. Additional annealing experiments were done at 500 and 800 °C for 6 h at 1 bar, Figure S8 (Supporting Information). The 3-layer systems displays no sign of oxidation at 500 °C, however, the sample annealed at 800 °C clearly shows the presence of IrO_2 peaks (110) at 28.1° and (220) at 57.9°, Figure S7 (Supporting Information). On further increasing the temperature to 1000 °C the IrO_2 transforms into volatile IrO_3 and sublimates. To test the thermal endurance of the 3-layer system from a practical application point of view,

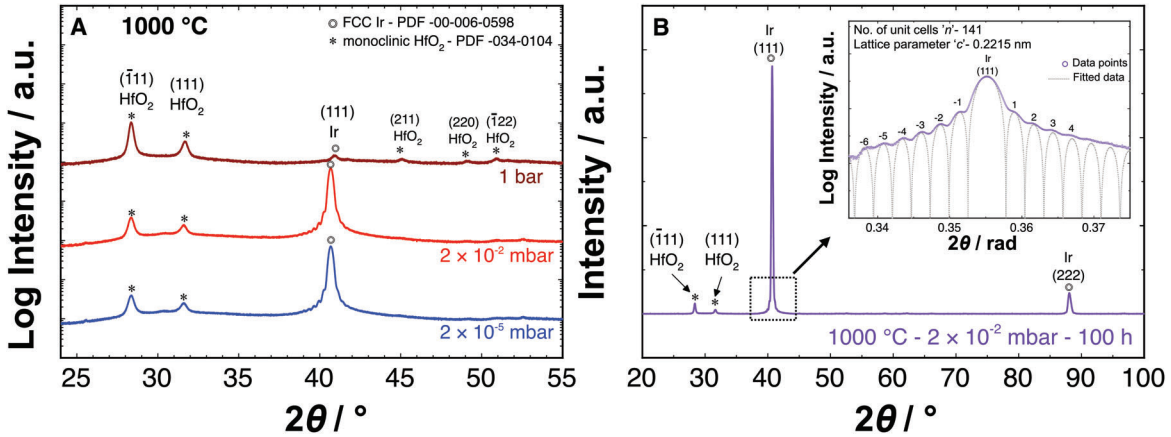

Figure 5. A) Background normalized diffraction patterns of a 3-layer system measured at room temperature, after ex situ annealing at 1000 °C for 6 h at 1 bar and different vacuum pressures. B) Diffraction pattern of a 3-layer system annealed at 1000 °C for 100 h at 2×10^{-2} mbar, the inset shows the presence of higher order satellite peaks due to coherent scattering and sharp interfaces between the layers.

© 2023 The Authors. Advanced Materials published by Wiley-VCH GmbH

15214095, 2023, 41, Downloaded from https://onlinelibrary.wiley.com/doi/10.1002/adma.202305922 by Technische Universität Hamburg Bibliothek - Elektronische Medien, Wiley Online Library on [23/11/2023]. See the Terms and Conditions (https://onlinelibrary.wiley.com/terms-and-conditions) on Wiley Online Library for rules of use; OA articles are governed by the applicable Creative Commons License

15214095, 2023, 41, Downloaded from https://onlinelibrary.wiley.com/doi/10.1002/adma.202305922 by Technische Universität Hamburg Bibliothek - Elektronische Medien, Wiley Online Library on [23/11/2023]. See the Terms and Conditions (https://onlinelibrary.wiley.com/terms-and-conditions) on Wiley Online Library for rules of use; OA articles are governed by the applicable Creative Commons License

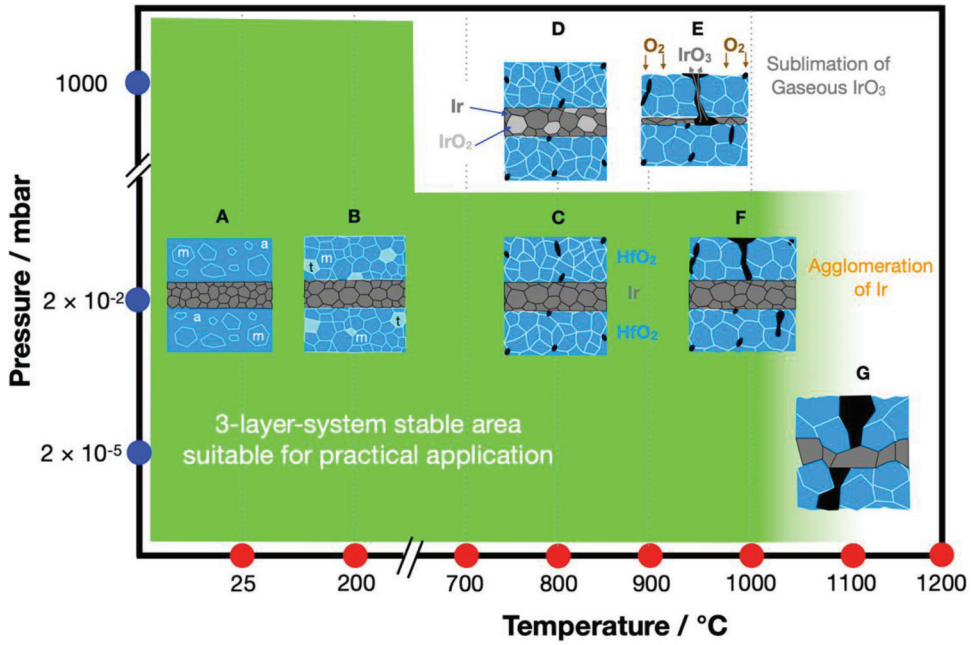

Figure 6. Scheme for clarification of the mechanisms and changes in a 3-layer system with a 30 nm-thick Ir layer sandwiched by two HfO_2 layers at different temperatures and pressure ranges: A) as-prepared 3-layer system: Ir is FCC with a grain size of 12 nm; HfO_2 exists in two phases: amorphous (a) and monoclinic (m); B) at 200 °C, phase transformation of HfO_2: amorphous (a) to tetragonal (t) occurs; grains are increasing; C) after 800 °C, second irreversible transformation of HfO_2: tetragonal (t) to monoclinic (m) happens; voids are formed and start to agglomerate at the grain boundary; further grain coarsening: Ir grain size attains the Ir layer thickness; top HfO_2 layer prevents agglomeration and interfacial broadening; D) at 1 bar, Ir layer is partially oxidized into IrO_2; oxygen reaches the Ir layer through generated transport channels; HfO_2 phase is now stable; E) above 800 °C at 1 bar, IrO_2 transforms into volatile IrO_3 and sublimates through the generated transport channels; HfO_2 phase is now stable; F) at low vacuum pressures; Ir layer is stable with sharp interfaces to HfO_2; lateral growth of Ir grains; no loss or oxidation of Ir through channels along the grain boundaries; G) structural perfection weakens, interfacial roughness increases, Ir grain size exceeds 30 nm, and the layer structure starts to degrade due to agglomeration. The zone in green represents the area, where the 3-layer system can perform efficiently for a duration over 100 h.

annealing measurements were performed at 1000 °C for 100 h at 2×10^{-2} mbar, in Figure 5B no sign of oxidation (absence of IrO_2 peaks) is evident even after this long annealing time. Moreover, the annealing leads to an improved structural perfection of the Ir layer. The (111) Ir peak highlighted by a black dotted box contains more minor oscillations at the foot of the peak. The oscillations are distinctly visible in the inset containing intensity plotted in the log scale. These oscillations are satellite peaks from the primary (111) Ir Bragg peak, which are formed above 800 °C due to crystalline coherence and a sharp interface between the top and bottom Ir/HfO_2 interfaces. In the as-prepared sample, they are absent. The peaks in the inset are fitted using the following function[109] shown below:

$$I(\theta) \propto \left[\left(\frac{\sin\left(\frac{\pi\, n\, c \sin\theta}{\lambda}\right)}{\sin\left(\frac{\pi\, c \sin\theta}{\lambda}\right)}\right)\right]^2 \quad (2)$$

where c is the lattice parameter in the out-of-plane direction, n is the number of unit cells that can be accommodated in the out-of-plane direction, λ is the wavelength of X-rays (for Cu_α radiation: $\lambda = 0.15046$ nm), and θ is the Bragg angle in radians. The lattice parameter c is 0.2215 nm and the number of unit cells n is 141, for the 3-layer system annealed at 1000 °C for 100 h at 2×10^{-2} mbar. The product of these two parameters can be used to calculate the thickness of the film,[110] which coincides with the 30 nm out-of-plane grain size shown in Figure 3A. This indicates that the grains in the out-of-plane direction extend to the full layer thickness of Ir. Satellite peaks can be used as a critical marker to determine the stability of the layer structure in a 3-layer system using X-ray diffraction. A change in peak position and reduction of higher-order peaks indicates a change in film thickness or loss of coherence due to agglomeration of Ir, which takes place at higher temperatures above 1100 °C.

A summary of the thermal endurance at different temperatures and pressure ranges for the 3-layer system is composed in **Figure 6**. Due to high-temperature annealing, long-term changes such as phase transformation, relaxation, and grain coarsening are emerging, but these effects are counterbalanced by the advanced 3-layer system of $HfO_2/Ir/HfO_2$ since the noble metal Ir is stable. Furthermore, the sharp interfaces with low roughness indicate a clear control of the tendency for agglomeration of the metal in a certain temperature-vacuum pressure area (green zone). The white zone indicates an area where the 3-layer system is unstable. Two different mechanisms are revealed. At ambient pressure (1 bar) above 800 °C, the dominant mechanism is the oxidation of Ir forming volatile oxides, whereas, at technical vacuum conditions and below, the dominant mechanism is grain growth in the Ir layer. The limit of the positive effect of additional interfaces, also shown in the bilayer experiments, becomes clear at very high temperatures. However, in the 3-layer system prior

© 2023 The Authors. Advanced Materials published by Wiley-VCH GmbH

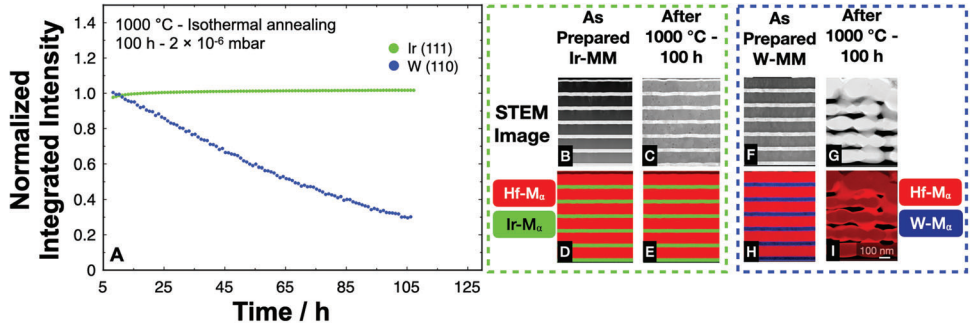

Figure 7. A) Normalized integrated intensity of (111) FCC Ir and (110) BCC W Bragg peaks during isothermal annealing as a function of time annealed over 100 h at 1000 °C in a pressure of 2×10^{-6} mbar. B–I) STEM-EDS analysis of the Ir/HfO_2 and W/HfO_2 metamaterial, as-prepared and annealed at 1000 °C for 100 h. B,C) STEM-HAADF images of Ir/HfO_2 metamaterial as-prepared and after annealing at 1000 °C, D,E) Ir-M_α (green) and Hf-M_α (red) mix elemental mapping, F,G) STEM-HAADF images of W/HfO_2 metamaterial as-prepared and after annealing at 1000 °C, H,I) W-M_α (blue) and Hf-M_α (red) mix elemental mapping. All the images have the same scale as indicated in (I).

to this limit, a reaction equilibrium state of solid Ir, its solid oxide IrO_2, and gaseous O_2 is established at high temperatures and in the low vacuum pressure region, which apparently reduces the strong negative influence of oxidation on the lifetime of selective emitter layers by the use of noble-metal iridium, which brings us to the following comparison.

After testing the 3-layer system at different pressures and temperatures, a multilayered metamaterial selective emitter, cap layer – HfO_2 100 nm/6 × (Ir 30 nm/HfO_2 100 nm)/bottom Ir layer 200 nm/sapphire, was fabricated and tested for long-term stability **Figure 7**. This metamaterial was designed to obtain high absorptivities/emissivities above the bandgap of the InGaAsSb PV cell at 0.55 eV, with a cut-off wavelength of 2.25 µm and low absorptivities/emissivities below the bandgap of the PV cell, **Figure 8**. In situ, annealing experiments were performed at 1000 °C for 100 h at 2×10^{-6} mbar to study the thermal endurance and check the influence of oxidation of both the metals in a multilayered metamaterial selective emitter. In X-ray diffraction, the integrated intensity of a diffraction peak of a particular phase depends on the content of this phase. In this experiment, any relative change in the integral over the peak intensity is directly proportional to a change in the metal volume fraction in the multilayered metamaterial selective emitter. It is worthwhile to mention that the second phase of monoclinic HfO_2 serves as a reference as it remains unaltered. Figure 7A shows the integrated intensity of (111) FCC Ir and (110) BCC W as a function of time during the isothermal annealing at 1000 °C. The intensity of Ir is almost stable over the entire duration, whereas a gradual drop in intensity is observed for W due to oxidation and later sublimation of volatile WO_x. The XRD results are also validated by the STEM-EDS measurements, Figure 7D,E,H,I. The Ir/HfO_2 metamaterial looks unaltered (Figure 7C,E) in comparison to the as-prepared sample, there is no sign of any oxidation in the Ir layer, or interdiffusion between the Ir/HfO_2 layers or agglomeration of Ir after 100 h. However, in the W/HfO_2 there is almost no signal from the W layer left after 100 h (Figure 7G,I), as the W layer oxidized and the formed oxide sublimated. Furthermore, an increased roughness is observed in the HfO_2 layers at the former interfaces. Figure 8 shows the absorptivity/emissivity spectra of the metamaterial emitter before and after annealing at 1000 °C, for 100 h under 2×10^{-6} mbar vacuum pressure. The as-fabricated metamaterial emitter shows a sharp decline in the absorptivities/emissivities around the cut-off wavelength, leading to below 10% absorptivity/emissivity at longer wavelengths. After annealing the emitter for 100 h, reduced absorptivities/emissivities are observed above the cut-off wavelength of the spectral region. The increase in Ir grain size, Figure 3, reduces the volume fraction of atoms in the grain boundaries and limits the electron scattering at the grain boundaries, as observed also elsewhere.[91] This, in turn, reduces the electron collision frequency of the metal and subsequently reduces absorptivity/emissivity at longer wavelengths. The application of such a selective emitter would allow increasing the spectral efficiency of a TPV system versus a black-body emitter from 19% to 52%, Figure S9 (Supporting Information). Furthermore, Figure S9B (Supporting Information) clearly indicates that the conversion efficiency of a selective emitter increases if higher temperatures are paired with larger-bandgap PV cells. Additionally, the thermal stability of the emitter for long durations and the resilience of the emitter

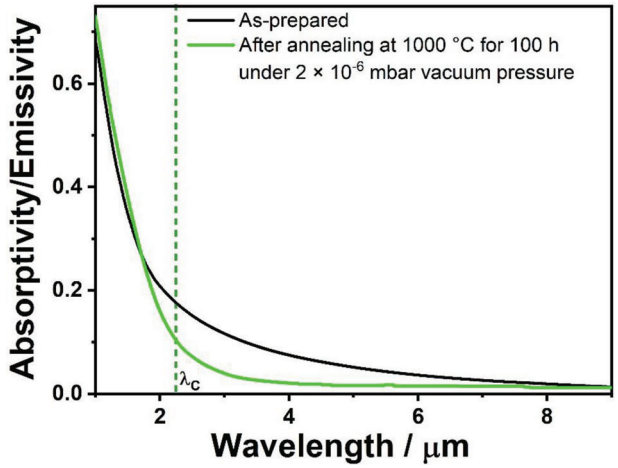

Figure 8. Experimental absorptivity/emissivity spectra of the ex situ annealed metamaterial, where λ_C is the cut-off wavelength of the InGaAsSb PV cell at 2.25 µm.

© 2023 The Authors. Advanced Materials published by Wiley-VCH GmbH

15214095, 2023, 41, Downloaded from https://onlinelibrary.wiley.com/doi/10.1002/adma.202305922 by Technische Universität Hamburg Bibliothek - Elektronische Medien, Wiley Online Library on [23/11/2023]. See the Terms and Conditions (https://onlinelibrary.wiley.com/terms-and-conditions) on Wiley Online Library for rules of use; OA articles are governed by the applicable Creative Commons License

15214095, 2023, 41, Downloaded from https://onlinelibrary.wiley.com/doi/10.1002/adma.202305922 by Technische Universität Hamburg Bibliothek - Elektronische Medien, Wiley Online Library on [23/11/2023]. See the Terms and Conditions (https://onlinelibrary.wiley.com/terms-and-conditions) on Wiley Online Library for rules of use; OA articles are governed by the applicable Creative Commons License

to multiple thermal cycles is shown in Figures S10 and S11 (Supporting Information). The above experiments demonstrate that Ir is a promising step to develop selective emitters for TPV energy-harvesting applications operating at feasible vacuum conditions.

3. Conclusion

TPV systems require a selective emitter to operate at high temperatures for a long duration. We demonstrate the thermal stability and oxidation resistance of Ir nanolayer sandwiched between HfO_2 layers by in situ and ex situ XRD annealing experiments. Oxidation of Ir above 1000 °C is prevented due to positive Gibbs energy of oxide formation. Temperature-induced grain growth in the Ir layer takes place, but the structural perfection of the interface is retained up to 1000 °C under moderate and low vacuum conditions and can be validated by the presence of satellite peaks. During annealing, the HfO_2 layers undergo phase transitions combined with void formation and their nanocrystalline grains are coarsened. Despite these changes, it is worthwhile mentioning that the system continues to meet the selective emission for TPV applications. In order to avoid possible oxidation of the iridium layers, annealing at 1000 °C was performed at a technical vacuum pressure of 2×10^{-2} mbar, as under this pressure, oxide formation is not thermodynamically favored anymore. During temperature ramp-up, Ir layers will be effectively protected from oxygen access by the adjacent comparatively thick HfO_2 layers. Another strategy that can be implemented is to quickly ramp-up from room temperature to 1000 °C and keep the pressure as low as possible ($\approx 10^{-6}$ mbar) in order to skip the temperature range favoring the formation of IrO_2.

A comparison at 1000 °C and over 100 h between an Ir and a W selective emitter supports our findings and reveals the superior oxidation resistance of the noble metal Ir. It also shows that probably all oxidizing refractory metals cannot be used as nanostructured metamaterials even if small quantities of oxygen are present. Future work will be focused on inhibiting agglomeration of the Ir layers by choice of other dielectric coatings such as hafnia. Higher temperatures above 1000 °C will allow to increase the radiated power of a TPV emitter and will further increase the oxidation resistance of the Ir-layers.

4. Experimental Section

Magnetron Sputtering: The bilayers, 3-layer systems, and metamaterials used in the annealing experiments were prepared at the Helmholtz Zentrum Hereon, using the in-house designed sputtering facility. The base pressure of the ultrahigh vacuum chamber was below 1×10^{-7} mbar. The coatings were deposited on sapphire substrates 8 mm × 8 mm × 0.5 mm having (1-102) orientation and 20 mm × 20 mm silicon substrates having (100) orientation. A custom-made sample holder rotating at 1 Hz was mounted at a distance of 14 cm from the sputtering source. The Ir and HfO_2 sputtering targets used were 3″ in diameter and have a high purity of 99.95%. The pressure during the sputtering process was maintained at 2×10^{-3} mbar using argon gas (7.0) with a flow of 28 sccm. The HfO_2 layers were coated using RF power of 400 W, which yielded a deposition rate of 0.15 nm s^{-1} and the Ir layers were coated using DC power of 100 W with a deposition rate of 0.12 nm s^{-1}. A 3-layer system was deposited in 40 min. Throughout the deposition, the sample holder was not cooled, and the sample temperature stayed under 100 °C, as determined by a thermocouple placed behind the sample.

X-ray Diffraction: All the in situ annealing measurements were performed in a diffractometer (Bruker D8 Advance) equipped with a heating stage (Anton Paar HTK 2000N) and a state-of-the-art position-sensitive detector (LynxEye XE-T) having a resolution of 380 eV. Temperature calibrations were done by annealing an uncoated sapphire substrate until 1900 °C in steps of 100 °C, with a heating rate of 25 °C min^{-1}. A full pattern fit from 50 to 125 °C was done on the annealed sapphire data using Rietveld analysis with the help of TOPAS software. The thermal coefficients of sapphire were estimated by comparing the experimental results of Touloukian et al.[111] Before annealing the heating chamber was evacuated to a pressure less than 3×10^{-6} mbar. The height of the *z*-stage was precisely adjusted to match the peak positions of the sapphire substrate with the powder diffraction file (PDF 01-082-1468) as the reference. During annealing experiments, the offset coupled θ–2θ scans (diffractograms) were measured between 20° to 50°, with an increment of 0.02° and a time of 0.1 s per step, using Cu $K_{\alpha 1}$ radiation ($\lambda = 0.15406$ nm). All the in situ annealing measurements, heating and cooling ramps, were done at a rate of 2 °C min^{-1}. The time between successive scans during the isothermal annealing was 8 min.

All ex situ measurements were performed in a diffractometer (Bruker D8 Advance) equipped with a compact cradle equipped with an air scatter and detector (LynxEye XE-T). The height of the z-stage was precisely adjusted to match the peak positions of the sapphire substrate with the powder diffraction file (PDF 01-082-1468) as the reference. The diffractograms were measured between 20° to 100°, with an increment of 0.2° and a time of 4 s per step, using Cu $K_{\alpha 1}$ radiation.

X-ray Reflectivity: The thickness, roughness, and density of 30 nm Ir, 100 nm HfO_2, bilayers, and 3-layer system were investigated with XRR using Cu $K_{\alpha 1}$ radiation ($\lambda = 0.15406$ nm) on silicon substrates prepared from the same sputtering run as the sapphire substrates. Reflection scans were recorded on a D8 Advance Bruker diffractometer equipped with a reflectometry stage, a knife-edge, and Göbel mirrors behind the source to shape parallel beams and monochromatize X-rays. The XRR scans were recorded between 0° and 6°, with an increment of 0.01° and a time of 10 s per step. Layer properties were investigated using LEPTOS R software from Bruker.

Ex Situ Annealing: Thermal annealing of the 3-layer system was done in a high-temperature vacuum furnace (RD-G WEBB) at a pressure of 2×10^{-2} mbar. A second set-up for annealing was done using a high-temperature heating stage (Linkam, TS 1500) at 2×10^{-2} and 2×10^{-5} mbar using a rough vacuum pump and a turbomolecular pump. The third set-up was done at 1 bar using a high-temperature Carbolite furnace (HTF 1700). The heating and cooling rate of the annealing experiments was 10 °C min^{-1}.

Atomic Force Microscopy: AFM high-resolution topography image of the as-prepared sample was obtained using SAA-HPI-SS probes (Bruker) with a nominal tip radius of 1 nm, spring constant of 0.25 N m^{-1} and resonance frequency of 55 kHz. Low peak force of 500 pN as well as a low tip velocity of 3.0 µm s^{-1} were used. For c-AFM measurements on the bilayer Ir/HfO_2 after annealing at 1000 °C for 6 h, an electrical contact between the sample and the AFM chuck was achieved using copper tape. Measurements were conducted using SCM-PIT-V2 probes (Bruker) with a nominal tip radius of 25 nm, spring constant of 3 N m^{-1} and resonance frequency of 75 kHz. A peak force of 25 nN was applied, and the tip velocity was set to 2.00 µm s^{-1}. During current measurements, a DC bias of +1.0 V was applied to the sample.

TEM and EDS Characterization: A focused-ion beam scanning electron microscope (FIB-SEM, FEI Helios G3 UC) instrument using a 30 keV gallium ion beam was used to prepare the cross-sectional TEM structures of the metamaterials, and the lamella was transferred to Cu lift-out grids. A protective layer of C was deposited onto the metamaterial to prevent charging during the lamella preparation. STEM images were acquired with an FEI Talos F200X TEM equipped with a high-brightness Schottky-FEG (X-FEG) detector. For EDS analyses, a four-quadrant SDD-EDS system (solid angle of 0.9 srad) was used. Spectrum images of 512 × 512 pixels were obtained with a probe current of 1 nA and a dwell time of 10 µs per pixel. Thermo Fischer Scientific Velox software was used for data acquisition and

© 2023 The Authors. Advanced Materials published by Wiley-VCH GmbH

visualization. For the spectrum images, the energies of the following elements were used: Al-K_α (1.49 keV), O-K_α (0.52 keV) Hf-M_α (1.64 keV), and Ir-M_α (1.77 keV).

Reflection Measurements (FTIR): Reflectivity spectra of the multilayered metamaterial were measured using a Fourier transform infrared (FTIR) spectrometer in the wavelength range of 1 to 10 µm. An FTIR microscope (Bruker Hyperion 2000) coupled to an FTIR spectrometer (Bruker Vertex 70) was used to measure the reflectivity, where a Schwarzschild objective with a magnification of 15 times was used to collect the light. The objective operated at ≈16° off-normal to the substrate surface and had a collection cone apex angle of ±7°. An Au mirror was used for normalization.

Supporting Information

Supporting Information is available from the Wiley Online Library or from the author.

Acknowledgements

The authors gratefully acknowledge financial support from the German Research Foundation (DFG) via SFB 986 "Tailor-Made Multi-Scale Materials Systems: M3", Project-ID 192346071, and projects C1 and Z3. The authors appreciate the support from the Helmholtz-Zentrum Hereon library.

Open access funding enabled and organized by Projekt DEAL.

Conflict of Interest

The authors declare no conflict of interest.

Data Availability Statement

The data that support the findings of this study are available from the corresponding author upon reasonable request.

Keywords

hafnia, iridium, magnetron sputtering, selective emitters, thermophotovoltaics, thin-films

Received: June 19, 2023
Revised: August 8, 2023
Published online: September 8, 2023

[1] R. E. Nelson, *Semicond. Sci. Technol.* **2003**, *18*, S141.
[2] T. J. Coutts, *Renewable Sustainable Energy Rev.* **1999**, *3*, 77.
[3] C. Ferrari, F. Melino, M. Pinelli, P. Spina, M. Venturini, *Energy Procedia* **2014**, *45*, 160.
[4] Y. Wang, H. Liu, J. Zhu, *APL Mater.* **2019**, *7*, 080906.
[5] T. Bauer, *Thermophotovoltaics: Basic Principles and Critical Aspects of System Design*, Springer Science & Business Media, Heidelberg, Germany **2011**.
[6] R. M. Swanson, in 1978 Int. Electron Devices Meeting, IEEE, Piscataway, NJ, USA, **1978**, pp. 70.
[7] Z. Omair, G. Scranton, L. M. Pazos-Outón, T. P. Xiao, M. A. Steiner, V. Ganapati, P. F. Peterson, J. Holzrichter, H. Atwater, E. Yablonovitch, *Proc. Natl. Acad. Sci. USA* **2019**, *116*, 15356.
[8] S. Molesky, C. J. Dewalt, Z. Jacob, *Opt. Express* **2013**, *21*, A96.
[9] J. Li, M. M. Hossain, B. Jia, D. Buso, M. Gu, *Opt. Express* **2010**, *18*, 4491.
[10] E. Rephaeli, S. Fan, *Opt. Express* **2009**, *17*, 15145.
[11] X. Liu, T. Tyler, T. Starr, A. F. Starr, N. M. Jokerst, W. J. Padilla, *Phys. Rev. Lett.* **2011**, *107*, 045901.
[12] N. A. Pfiester, T. E. Vandervelde, *Phys. Status Solidi A* **2017**, *214*, 1600410.
[13] Z. Wang, D. Kortge, Z. He, J. Song, J. Zhu, C. Lee, H. Wang, P. Bermel, *Sol. Energy Mater. Sol. Cells* **2022**, *238*, 111554.
[14] D. Chubb, *Fundamentals of Thermophotovoltaic Energy Conversion*, Elsevier, Amsterdam, The Netherlands **2007**.
[15] M. Planck, *The Theory of Heat Radiation*, P. Blakiston's Son & Co, Philadelphia, PA, USA **1914**.
[16] A. LaPotin, K. L. Schulte, M. A. Steiner, K. Buznitsky, C. C. Kelsall, D. J. Friedman, E. J. Tervo, R. M. France, M. R. Young, A. Rohskopf, S. Verma, E. N. Wang, A. Henry, *Nature* **2022**, *604*, 287.
[17] T. C. Narayan, L. Y. Kuritzky, D. P. Nizamian, B. A. Johnson, E. J. Tervo, A. R. Young, C. Luciano, M. K. Arulanandam, B. M. Kayes, E. E. Perl, M. Limpinsel, P. Santhanam, J. Slack, W. Olavarria, J. Carapella, M. Young, C. L. Wu, Z. J. Yu, Z. C. Holman, R. R. King, M. A. Steiner, D. M. Bierman, A. J. Ponec, J. A. Briggs, in 2020 47th IEEE Photovoltaic Specialists Conf. (PVSC), IEEE Piscataway, NJ, USA **2020**, pp. 1792–1795.
[18] D. N. Woolf, E. A. Kadlec, D. Bethke, A. D. Grine, J. J. Nogan, J. G. Cederberg, D. B. Burckel, T. S. Luk, E. A. Shaner, J. M. Hensley, *Optica* **2018**, *5*, 213.
[19] D. Fan, T. Burger, S. McSherry, B. Lee, A. Lenert, S. R. Forrest, *Nature* **2020**, *586*, 237.
[20] B. Roy-Layinde, T. Burger, D. Fan, B. Lee, S. McSherry, S. R. Forrest, A. Lenert, *Sol. Energy Mater. Sol. Cells* **2022**, *236*, 111523.
[21] S. McSherry, M. Webb, J. Kaufman, Z. Deng, A. Davoodabadi, T. Ma, E. Kioupakis, K. Esfarjani, J. T. Heron, A. Lenert, *Nat. Nanotechnol.* **2022**, *17*, 1104.
[22] L. Mao, H. Ye, *Renewable Energy* **2010**, *35*, 249.
[23] D. M. Bierman, A. Lenert, W. R. Chan, B. Bhatia, I. Celanović, M. Soljačić, E. N. Wang, *Nat. Energy* **2016**, *1*, 16068.
[24] A. Lenert, Y. Nam, D. M. Bierman, E. N. Wang, *Opt. Express* **2014**, *22*, A1604.
[25] P. N. Dyachenko, S. Molesky, A. Y. Petrov, M. Störmer, T. Krekeler, S. Lang, M. Ritter, Z. Jacob, M. Eich, *Nat. Commun.* **2016**, *7*, 11809.
[26] M. Shimizu, T. Furuhashi, Z. Liu, H. Yugami, *Sol. Energy Mater. Sol. Cells* **2022**, *245*, 111878.
[27] M. Shimizu, A. Kohiyama, H. Yugami, *J. Quant. Spectrosc. Radiat. Transfer* **2018**, *212*, 45.
[28] R. Sakakibara, V. Stelmakh, W. Chan, M. Ghebrebrhan, J. Joannopoulos, M. Soljacic, I. Čelanović, *J. Photonics Energy* **2019**, *9*, 032713.
[29] T. Burger, C. Sempere, B. Roy-Layinde, A. Lenert, *Joule* **2020**, *4*, 1660.
[30] D. G. Baranov, Y. Xiao, I. A. Nechepurenko, A. Krasnok, A. Alù, M. A. Kats, *Nat. Mater.* **2019**, *18*, 920.
[31] A. Licht, N. Pfiester, D. DeMeo, J. Chivers, T. E. Vandervelde, *MRS Adv.* **2019**, *4*, 2271.
[32] Z. Zhou, E. Sakr, Y. Sun, P. Bermel, *Nanophotonics* **2016**, *5*, 1.
[33] M. Oh, J. McElearney, A. Lemire, T. E. Vandervelde, *Phys. Rev. Mater.* **2022**, *6*, 110201.
[34] R. Sakakibara, V. Stelmakh, W. R. Chan, R. D. Geil, S. Krämer, T. Savas, M. Ghebrebrhan, J. D. Joannopoulos, M. Soljačić, I. Čelanović, *Sol. Energy Mater. Sol. Cells* **2022**, *238*, 111536.
[35] N. Jeon, J. J. Hernandez, D. Rosenmann, S. K. Gray, A. B. F. Martinson, J. J. Foley IV, *Adv. Energy Mater.* **2018**, *8*, 1801035.
[36] S. Shan, C. Chen, P. G. Loutzenhiser, D. Ranjan, Z. Zhou, Z. M. Zhang, *Front. Energy* **2020**, *14*, 482.
[37] A. Lenert, D. M. Bierman, Y. Nam, W. R. Chan, I. Celanović, M. Soljačić, E. N. Wang, *Nat. Nanotechnol.* **2014**, *9*, 126.

© 2023 The Authors. Advanced Materials published by Wiley-VCH GmbH

15214095, 2023, 41, Downloaded from https://onlinelibrary.wiley.com/doi/10.1002/adma.202305922 by Technische Universität Hamburg Bibliothek - Elektronische Medien, Wiley Online Library on [23/11/2023]. See the Terms and Conditions (https://onlinelibrary.wiley.com/terms-and-conditions) on Wiley Online Library for rules of use; OA articles are governed by the applicable Creative Commons License

[38] M. Chirumamilla, G. V. Krishnamurthy, K. Knopp, T. Krekeler, M. Graf, D. Jalas, M. Ritter, M. Störmer, A. Y. Petrov, M. Eich, *Sci. Rep.* **2019**, *9*, 7241.
[39] V. Rinnerbauer, S. Ndao, Y. X. Yeng, W. R. Chan, J. J. Senkevich, J. D. Joannopoulos, M. Soljačić, I. Celanovic, *Energy Environ. Sci.* **2012**, *5*, 8815.
[40] K. A. Arpin, M. D. Losego, A. N. Cloud, H. Ning, J. Mallek, N. P. Sergeant, L. Zhu, Z. Yu, B. Kalanyan, G. N. Parsons, G. S. Girolami, J. R. Abelson, S. Fan, P. V. Braun, *Nat. Commun.* **2013**, *4*, 2630.
[41] A. Chirumamilla, F. Ding, Y. Yang, M. S. Mani Rajan, S. I. Bozhevolnyi, D. S. Sutherland, K. Pedersen, M. Chirumamilla, *Sol. Energy Mater. Sol. Cells* **2023**, *259*, 112449.
[42] M. G. Mauk, V. M. Andreev, *Semicond. Sci. Technol.* **2003**, *18*, S191.
[43] M. Tan, L. Ji, Y. Wu, P. Dai, Q. Wang, K. Li, T. Yu, Y. Yu, S. Lu, H. Yang, *Appl. Phys. Express* **2014**, *7*, 096601.
[44] W. Shockley, H. J. Queisser, *J. Appl. Phys.* **2004**, *32*, 510.
[45] A. Cabrera, A. Ramos, I. Artacho, M. Gomez, K. Gavin, A. Martí, A. Datas, in 2018 Spanish Conf. on Electron Devices (CDE), IEEE, Piscataway, NJ, USA **2018**, https://doi.org/10.1109/CDE.2018.8596820.
[46] H. Nils-Peter, W. Peter, *Semicond. Sci. Technol.* **2003**, *18*, S151.
[47] E. Blandre, R. Vaillon, J. Drévillon, *Opt. Express* **2019**, *27*, 36340.
[48] B. Wernsman, R. G. Mahorter, R. Siergiej, S. D. Link, R. J. Wehrer, S. J. Belanger, P. Fourspring, S. Murray, F. Newman, D. Taylor, T. Rahmlow, *AIP Conf. Proc.* **2005**, *746*, 1441.
[49] K. Chen, P. Santhanam, S. Fan, *Appl. Phys. Lett.* **2015**, *107*, 091106.
[50] B. Heeg, J.-B. Wang, S. Johnson, B. Buckner, Y.-H. Zhang, Proc. SPIE **2007**, 6461, 64610K.
[51] L. M. Fraas, J. E. Avery, H. X. Huang, *Semicond. Sci. Technol.* **2003**, *18*, S247.
[52] M. Bianchi, C. Ferrari, F. Melino, A. Peretto, *Appl. Energy* **2012**, *97*, 704.
[53] K. F. Mustafa, S. Abdullah, M. Z. Abdullah, K. Sopian, *Renewable Sustainable Energy Rev.* **2017**, *71*, 572.
[54] W. R. Chan, V. Stelmakh, M. Ghebrebrhan, M. Soljačić, J. D. Joannopoulos, I. Čelanović, *Energy Environ. Sci.* **2017**, *10*, 1367.
[55] D. Jiang, W. Yang, A. Tang, *Energy Convers. Manag.* **2015**, *103*, 359.
[56] W. R. Chan, P. Bermel, R. C. Pilawa-Podgurski, C. H. Marton, K. F. Jensen, J. J. Senkevich, J. D. Joannopoulos, M. Soljačić, I. Celanovic, *Proc. Natl. Acad. Sci. USA* **2013**, *110*, 5309.
[57] T. Inoue, T. Koyama, D. D. Kang, K. Ikeda, T. Asano, S. Noda, *Nano Lett.* **2019**, *19*, 3948.
[58] A. Lochbaum, Y. Fedoryshyn, A. Dorodnyy, U. Koch, C. Hafner, J. Leuthold, *ACS Photonics* **2017**, *4*, 1371.
[59] H. Wang, X. Tang, Y. Liu, Z. Xu, Z. Yuan, K. Liu, Z. Zhang, T. Jiang, *Energy Technol.* **2020**, *8*, 1901170.
[60] V. L. Teofilo, P. Choong, J. Chang, Y. L. Tseng, S. Ermer, *J. Phys. Chem. C* **2008**, *112*, 7841.
[61] A. Datas, A. Martí, *Sol. Energy Mater. Sol. Cells* **2017**, *161*, 285.
[62] C. Amy, H. R. Seyf, M. A. Steiner, D. J. Friedman, A. Henry, *Energy Environ. Sci.* **2019**, *12*, 334.
[63] A. Datas, A. Ramos, A. Martí, C. del Cañizo, A. Luque, *Energy* **2016**, *107*, 542.
[64] https://antoraenergy.com/technology.Antora (accessed: August 2023).
[65] C. Amy, D. Budenstein, M. Bagepalli, D. England, F. DeAngelis, G. Wilk, C. Jarrett, C. Kelsall, J. Hirschey, H. Wen, A. Chavan, B. Gilleland, C. Yuan, W. C. Chueh, K. H. Sandhage, Y. Kawajiri, A. Henry, *Nature* **2017**, *550*, 199.
[66] G. Gottstein, *Physical Foundations of Materials Science*, Springer, Heidelberg, Germany **2004**.
[67] G. Gottstein, L. S. Shvindlerman, *Grain Boundary Migration in Metals: Thermodynamics, Kinetics, Applications*, CRC Press, Boca Raton, FL, USA **2009**.
[68] R. E. Reed-Hill, R. Abbaschian, L. Abbaschian, *Physical Metallurgy Principles*, Cengage Learning, New York, **1973**.
[69] I. L. Shabalin, I. L. Shabalin, *Ultra-High Temperature Materials I: Carbon (Graphene/Graphite) and Refractory Metals*, Springer, Heidelberg, Germany, **2014**.
[70] T. Krekeler, S. S. Rout, G. V. Krishnamurthy, M. Störmer, M. Arya, A. Ganguly, D. S. Sutherland, S. I. Bozhevolnyi, M. Ritter, K. Pedersen, A. Y. Petrov, M. Eich, M. Chirumamilla, *Adv. Opt. Mater.* **2021**, *9*, 2100323.
[71] V. Stelmakh, W. R. Chan, M. Ghebrebrhan, J. Senkevich, J. D. Joannopoulos, M. Soljačić, I. Celanović, *IEEE Trans. Nanotechnol.* **2016**, *15*, 303.
[72] A. Kohiyama, M. Shimizu, H. Yugami, *Appl. Phys. Express* **2016**, *9*, 112302.
[73] A. Narayanaswamy, J. Cybulski, G. Chen, *AIP Conf. Proc.* **2004**, *738*, 215.
[74] U. Guler, A. Boltasseva, V. M. Shalaev, *Science* **2014**, *344*, 263.
[75] M. Arya, A. Ganguly, G. V. Krishnamurthy, S. S. Rout, L. Gurevich, T. Krekeler, M. Ritter, K. Pedersen, M. Störmer, A. Y. Petrov, *Appl. Surf. Sci.* **2022**, *588*, 152927.
[76] A. Chirumamilla, Y. Yang, M. H. Salazar, F. Ding, D. Wang, P. K. Kristensen, P. Fojan, S. I. Bozhevolnyi, D. S. Sutherland, K. Pedersen, M. Chirumamilla, *Mater. Today Phys.* **2021**, *21*, 100503.
[77] M. Chirumamilla, A. Chirumamilla, Y. Yang, A. S. Roberts, P. K. Kristensen, K. Chaudhuri, A. Boltasseva, D. S. Sutherland, S. I. Bozhevolnyi, K. Pedersen, *Adv. Opt. Mater.* **2017**, *5*, 1700552.
[78] M. Chirumamilla, G. V. Krishnamurthy, S. S. Rout, M. Ritter, M. Störmer, A. Y. Petrov, M. Eich, *Sci. Rep.* **2020**, *10*, 3605.
[79] L. Hunt, *Platinum Met. Rev.* **1987**, *31*, 32.
[80] D. E. Gray, I. E. Dayton, *Am. J. Phys.* **1964**, *32*, 389.
[81] P. Atkins, L. Jones, *Chemical Principles: The Quest for Insight*, Macmillan Higher Education, UK **2007**.
[82] I. Barin, G. Platzki, *Thermochemical Data of Pure Substances*, VCH, Weinheim, Germany **1989**.
[83] E. Cordfunke, G. Meyer, *Recl. Trav. Chim. Pays-Bas* **1962**, *81*, 495.
[84] D. E. Peterson, *Thermodynamics and Transport of Gaseous Iridium Oxides in Multi-Hundred-Watt Thermoelectric Generators*, Los Alamos National Laboratory, Los Alamos, NM, USA **1976**.
[85] H. S. C. O'Neill, J. Nell, *Geochim. Cosmochim. Acta* **1997**, *61*, 5279.
[86] H. Jehn, *J. Less-Common Met.* **1984**, *100*, 321.
[87] S. Bai, L. Zhu, H. Zhang, Y. Ye, W. Gao, *Int. J. Refract. Met. Hard Mater.* **2013**, *41*, 563.
[88] R. T. Wimber, H. G. Kraus, *Metall. Trans.* **1974**, *5*, 1565.
[89] J. Norman, H. G. Staley, W. E. Bell, *J. Chem. Phys.* **1965**, *42*, 1123.
[90] M. Oh, E. S. Carlson, T. E. Vandervelde, *Comput. Mater. Sci.* **2021**, *197*, 110598.
[91] P. Schmitt, N. Felde, T. Döhring, M. Stollenwerk, I. Uschmann, K. Hanemann, M. Siegler, G. Klemm, N. Gratzke, A. Tünnermann, *Opt. Mater. Express* **2022**, *12*, 545.
[92] L. Yan, J. A. Woollam, *J. Appl. Phys.* **2002**, *92*, 4386.
[93] M. Störmer, F. Siewert, H. Sinn, *J. Synchrotron. Rad.* **2016**, *23*, 50.
[94] G. V. Krishnamurthy, M. Chirumamilla, S. S. Rout, K. P. Furlan, T. Krekeler, M. Ritter, H.-W. Becker, A. Y. Petrov, M. Eich, M. Störmer, *Sci. Rep.* **2021**, *11*, 3330.
[95] L. G. Parratt, *Phys. Rev.* **1954**, *95*, 359.
[96] D. T. Attwood, Soft X-rays and Extreme UV Radiation: Principles and Application, Cambridge University Press, New York **1999**.
[97] E. Spiller, *Soft X-ray Optics*, SPIE Press, Bellingham, WA, USA **1994**.
[98] A. Ulyanenkov, S. Sobolewski, *J. Phys. D: Appl. Phys.* **2005**, *38*, A235.
[99] F. H. Chung, R. W. Scott, *J. Appl. Crystallogr.* **1973**, *6*, 225.
[100] N. Wakelyn, P. Young, *J. Appl. Polym. Sci.* **1966**, *10*, 1421.
[101] H. P. Klug, L. E. Alexander, *X-ray Diffraction Procedures: For Polycrystalline and Amorphous Materials*, John Wiley & Sons, New York **1974**.

© 2023 The Authors. Advanced Materials published by Wiley-VCH GmbH

15214095, 2023, 41, Downloaded from https://onlinelibrary.wiley.com/doi/10.1002/adma.202305922 by Technische Universität Hamburg Bibliothek - Elektronische Medien, Wiley Online Library on [23/11/2023]. See the Terms and Conditions (https://onlinelibrary.wiley.com/terms-and-conditions) on Wiley Online Library for rules of use; OA articles are governed by the applicable Creative Commons License

[102] H. Gleiter, *Prog. Mater. Sci.* **1989**, *33*, 223.
[103] R. Birringer, H. Gleiter, H.-P. Klein, P. Marquardt, *Phys. Lett. A* **1984**, *102*, 365.
[104] F. Li, T. Liu, J. Zhang, S. Shuang, Q. Wang, A. Wang, J. Wang, Y. Yang, *Mater. Today Adv.* **2019**, *4*, 100027.
[105] A. Inoue, *Prog. Mater. Sci.* **1998**, *43*, 365.
[106] C. V. Thompson, *Annu. Rev. Mater. Res.* **2012**, *42*, 399.
[107] O. Elmazria, T. Aubert, *Proc. SPIE* **2011**, *8066*, 806602.
[108] D. R. Gaskell, D. E. Laughlin, *Introduction to the Thermodynamics of Materials*, CRC Press, Boca Raton, FL, USA **2017**.
[109] J.-M. Triscone, P. Fivat, M. Andersson, M. Decroux, *Phys. Rev. B* **1994**, *50*, 1229.
[110] J. A. Switzer, J. C. Hill, N. K. Mahenderkar, Y.-C. Liu, *ACS Appl. Mater. Interfaces* **2016**, *8*, 15828.
[111] Y. S. Touloukian, R. K. Kirby, R. E. Taylor, P. D. Desai, *Thermophys. Prop. Matter* **1975**, *13*, 5439716.

© 2023 The Authors. Advanced Materials published by Wiley-VCH GmbH

15214095, 2023, 41, Downloaded from https://onlinelibrary.wiley.com/doi/10.1002/adma.202305922 by Technische Universität Hamburg Bibliothek - Elektronische Medien, Wiley Online Library on [23/11/2023]. See the Terms and Conditions (https://onlinelibrary.wiley.com/terms-and-conditions) on Wiley Online Library for rules of use; OA articles are governed by the applicable Creative Commons License